Highlights

Implementation of isoconversional pyrolysis kinetics in a finite-element model of charring ablation

Kalid Kassa, Qasem Ahmed Drmosh, Sheriffdeen Anafi, Suhail Hyder Vattathurvalappil, Abrar H. Baluch

- FWO isoconversional kinetics implemented in Abaqus for charring ablation modeling
- User subroutines developed to couple conversion dependent kinetics with thermal response
- Multi rate TGA data incorporated into coupled thermal–pyrolysis ablation simulations
- Recession and surface temperature predictions improved over Arrhenius kinetics
- Model reproduces experimental ablation trends across multiple heating conditions

Implementation of isoconversional pyrolysis kinetics in a finite-element model of charring ablation

Kalid Kassa[a], Qasem Ahmed Drmosh[b], Sheriffdeen Anafi[a], Suhail Hyder Vattathurvalappil[a] and Abrar H. Baluch[a,c,*]

[a]Department of Aerospace Engineering, King Fahd University of Petroleum and Minerals, Dhahran, 31261, Eastern Province, Saudi Arabia
[b]Materials Science and Engineering Department, King Fahd University of Petroleum and Minerals, Dhahran, 31261, Eastern Province, Saudi Arabia
[b]IRC for Aviation and Space Exploration, King Fahd University of Petroleum and Minerals, Dhahran, 31261, Eastern Province, Saudi Arabia

ARTICLE INFO

Keywords:
Charring ablation
Isoconversional kinetics
Flynn–Wall–Ozawa (FWO)
Multi-rate TGA
Phenolic-impregnated carbon ablator
Finite element analysis (FEA)

ABSTRACT

Constant-parameter Arrhenius models for phenolic-impregnated carbon ablator (PICA) often match surface temperature, yet systematically overstate char recession. This study implements isoconversional kinetics extracted from multi-rate TGA via Flynn–Wall–Ozawa and embedded in `UMATHT` for PICA, with tabulated activation energy and pre-exponential factor $\{E(\alpha), A(\alpha)\}$ advanced at integration points and coupled to conduction, pyrolysis-gas enthalpy, radiative and convective exchange with blowing, and mesh motion. Validation against oxy-acetylene tests shows two main improvements: surface-temperature plateaus remain within the measured 2250–2500 K band while avoiding the Arrhenius overshoot, and mid-range predictions fall by 60–120 K toward the data. Recession bias is reduced by $\sim$ 39%, from up to fourteen-fold overprediction to $\sim$ 0.7–3.5× the experimental mean ($\approx 0.24\,\mathrm{mm\,s^{-1}}$). Joint interpretation of temperature history, recession-depth kinetics, and heating-rate fields shows a traveling subsurface maximum that weakens with time and reduces char consumption. Because a single convective coefficient cannot match both temperature and recession, boundary closure limits fidelity.

Acronyms

ALE	Arbitrary Lagrangian–Eulerian
FEM	Finite Element Method
FWO	Flynn–Wall–Ozawa isoconversional kinetic method
ICTAC	International Confederation for Thermal Analysis and Calorimetry
PICA	Phenolic-Impregnated Carbon Ablator
TGA	Thermogravimetric Analysis
TPS	Thermal Protection System
UMATHT	User MATerial Heat Transfer subroutine in ABAQUS

1. Introduction

It has proven difficult to formulate robust thermal protection layers for spacecraft re-entry. These layers shield internal structures from extreme aerodynamic heating, where surface temperatures may approach 3000 K [1]. Aluminum alloys cannot withstand such loads and are therefore protected by ablative materials such as phenolic-impregnated carbon ablator (PICA) [2–4]. During atmospheric entry, PICA absorbs heat as well as erodes through oxidation and vaporization, while the outer surface decomposes to form a protective char layer. Accurate ablation modeling requires a surface energy balance that includes radiative and convective heat transfer, pyrolysis-gas enthalpy, and surface recession, coupled with an in-depth conduction equation that accounts for decomposition. This framework underlies most charring-ablation solvers.

Several computational tools have been developed for this purpose. Early one-dimensional solvers such as FIAT and CMA used finite-difference or finite-volume methods to model coupled thermal, chemical, and structural response [5, 6]. Later extensions such as TITAN and 3D-FIAT incorporated multidimensional capabilities [7]. Academic FORTRAN/MATLAB and OpenFOAM solvers have been applied to AVCOAT, SIR-P, and porous carbon-phenolic systems [7–10]. Custom FEM tools (CHAR, HERO) improved geometric flexibility but were less accessible than commercial environments [5, 11–17]. More recently, ABAQUS has been adopted for ablation modeling through user subroutines and adaptive meshing that incorporate decomposition kinetics and track recession [18, 19]. However, nearly all ABAQUS implementations still use Arrhenius laws with pre-exponential factors $A(\alpha)$ and constant activation energy $E(\alpha)$. While straightforward, this assumption neglects the multi-step reactions of real PICA decomposition, causing good agreement with surface temperature but a systematic overprediction of char recession in oxy-acetylene tests [18]. No prior work has implemented isoconversional kinetics in ABAQUS, leaving this limitation unresolved.

Isoconversional methods determine kinetic parameters without assuming a single reaction path. The Flynn–Wall–Ozawa (FWO) method estimates activation energy across conversion levels using a logarithmic integral formulation; Kissinger refines temperature-integral evaluation; Friedman uses the differential rate; and Vyazovkin reduces errors from

---

[*] Corresponding author.
`abrar.baluch@kfupm.edu.sa` (A.H. Baluch)

Nomenclature

Roman & Greek symbols

B'	nondimensional recession parameter	–
B'_c	char blowing contribution	–
B'_g	pyrolysis–gas blowing contribution	–
C_p	specific heat capacity	J/(kg·K)
$C_{p,v}$	virgin specific heat	J/(kg·K)
$C_{p,c}$	char specific heat	J/(kg·K)
C_H	Stanton-type convection coefficient	kg/(m^{2}s)
$E(\alpha)$	activation energy (isoconversional)	J/mol
$f(\alpha)$	reaction model function	–
$g(\alpha)$	integrated reaction model	–
h	specific enthalpy	J/kg
$\bar{h}$	mixture-averaged enthalpy	J/kg
h_v, h_c	virgin/char enthalpies	J/kg
h_g	pyrolysis-gas enthalpy	J/kg
k	effective thermal conductivity	W/(m·K)
$\dot{m}_g$	pyrolysis–gas mass flux	kg/(m^{2}s)
p	pyrolysis–gas pressure	Pa
R	universal gas constant	8.314 J/(mol·K)
$\dot{s}$	surface recession rate	m/s
T	temperature	K
T_α	temperature at fixed conversion	K
t	time	s
U_e	external flow speed	m/s
y	in-depth coordinate	m
α	conversion fraction	–
β	heating rate	K/s
ρ	density	kg/m^3
ρ_v, ρ_c	virgin/char densities	kg/m^3
ρ_s	surface density	kg/m^3
σ	Stefan–Boltzmann constant	W/(m^{2}K^4)
ε	emissivity	–
$A(\alpha)$	pre-exponential factor (isoconversional)	s^{-1}

Subscripts

c	char state
e	freestream
g	pyrolysis gas
r	recovery
s	surface
v	virgin
w	wall
∞	ambient condition

varying heating rates. Among these, FWO is preferred for PICA one-dimensional pyrolysis simulations because it averages over temperature intervals, is less sensitive to noise, and easily incorporates multi-rate TGA data. By contrast, the EAS(Extended Arrhenius Scheme) method requires complex numerical integration, and Friedman is sensitive to noise [20–32].

In this work, we extend the ABAQUS-based finite-element ablation framework by replacing the Arrhenius law with an isoconversional formulation. Multi-rate TGA data of PICA resin were analyzed using the FWO method to extract conversion-dependent $E(\alpha)$ and $A(\alpha)$, which were incorporated into `UMATHT` so that decomposition evolves with conversion. The implementation is applied to the oxy-acetylene PICA test case to demonstrate that isoconversional kinetics improve the fidelity of FEM ablation simulations, maintaining correct surface-heating trends while reducing the long-standing overprediction of char recession.

2. Ablation phenomenon and governing equations

2.1. Ablation Phenomenon

During hypersonic reentry, spacecraft surfaces face extreme heating, and ablative materials such as phenolic-impregnated carbon ablator (PICA) act as sacrificial heat shields by absorbing this heat and protecting the spacecraft through controlled material erosion. Heat conducts inward and triggers thermal decomposition of the polymeric binder in the interior. As pristine material enters the pyrolysis zone, it breaks down into gases, volatile products, and carbon-based char residue. The gases move through the porous char layer, carrying away heat and influencing the energy balance at the surface. The remaining char layer protects the spacecraft, but oxidation and erosion gradually remove it and reduce its thickness. These combined processes define the charring ablation process.

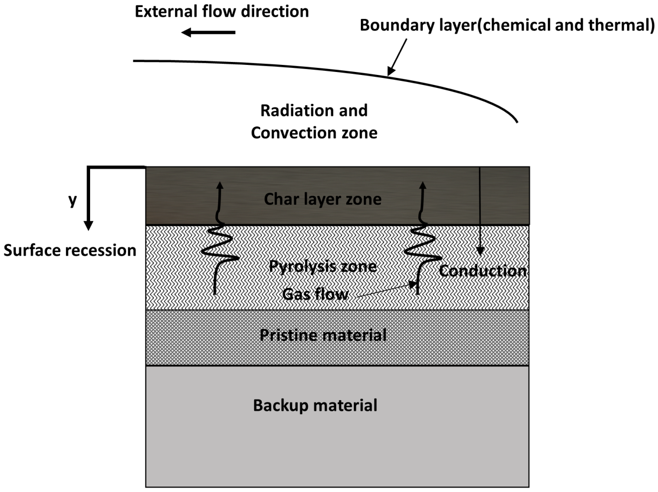

Figure 1: Schematic of the charring ablation process during re-entry

2.2. Governing equations for charring ablation with an Isoconversional (FWO) de-compositional law

The derivation collects a self-consistent set of field equations for a one-dimensional charring ablator written in a fixed spatial coordinate aligned with the surface normal.

The formulation follows the standard energy balance with conduction, pyrolysis-gas advection, and chemical-energy terms, standard surface boundary conditions, and a decomposition law based on isoconversional (Flynn–Wall–Ozawa, FWO) functions of conversion[33–40].

Let y denote the in-depth coordinate measured from the heated surface, $T(y,t)$ the temperature, $\rho(y,t)$ the local bulk density, and $\dot{s}(t)$ the surface recession speed. The composite is represented by two resin components (A, B) and one reinforcement (C). The bulk density obeys a linear mixture rule between resin and reinforcement:

$$\rho = \Gamma(\rho_A + \rho_B) + (1 - \Gamma)\rho_C \tag{1}$$

Here ρ is the bulk density, Γ is the resin fraction, ρ_A and ρ_B are resin component densities, and ρ_C is reinforcement density.

$$x = \frac{\rho_v}{\rho_v - \rho_c}\left(1 - \frac{\rho_c}{\rho}\right) \tag{2}$$

x denotes the virgin fraction ($0 \leq x \leq 1$). It provides a smooth transition between virgin and char states based on density evolution; ρ_v and ρ_c are the limiting virgin and char densities.

$$k = xk_v + (1-\delta)k_c, \qquad C_p = xC_{p,v} + (1-x)C_{p,c} \tag{3}$$

k and C_p are effective virgin- and char-state properties based on parallel conduction paths and local thermal equilibrium, with a rule-of-mixtures weighted by x ensuring stable property evolution.

The energy balance in the fixed coordinate includes storage, conduction, pyrolysis-gas advection, the latent-type chemistry term from in-depth decomposition, and the mesh-motion coupling term due to surface recession:

$$\bar{h}(T) = \frac{\rho_v h_v - \rho_c h_c}{\rho_v - \rho_c} \tag{4}$$

$\bar{h}(T)$ is mixture enthalpy; $h_v(T)$ and $h_c(T)$ are virgin and char solid-phase enthalpies.

$$\rho C_p \left.\frac{\partial T}{\partial t}\right|_y = \frac{\partial}{\partial y}\left(k\frac{\partial T}{\partial y}\right) + \dot{m}_g \frac{\partial h_g}{\partial y} + (h_g - \bar{h})\left.\frac{\partial \rho}{\partial t}\right|_y + \dot{s}\,\rho C_p \frac{\partial T}{\partial y} \tag{5}$$

For a porous control volume fixed in space, the net heat flux splits into conduction and gas-enthalpy flux, with mass conservation giving $\partial \dot{m}_g/\partial y = -\partial\rho/\partial t$, which groups into the chemistry term $(h_g - \bar{h})\partial\rho/\partial t$. Surface recession in a fixed (Eulerian) coordinate introduces the apparent solid-advection term $\dot{s}\rho C_p\,\partial T/\partial y$, yielding Eq. (5).

The in-depth mass flux of pyrolysis gas is the cumulative source from local decomposition; in one dimension it reduces to:

$$\dot{m}_g(y,t) = -\int_0^y \left.\frac{\partial \rho}{\partial t}\right|_\eta d\eta \tag{6}$$

At the heated boundary, the blown convective heat flux, radiative exchange, and the enthalpy carried by pyrolysis gas and char removal determine the wall gradient. Using normalized mass-transfer parameters,

$$\begin{aligned} -k \left.\frac{\partial T}{\partial y}\right|_w &= \rho_e U_e C_H \left(B'_c h_c + B'_g h_g - B' h_w\right) \\ &\quad + \rho_e U_e C_H (h_r - h_w) - \sigma\varepsilon(T_w^4 - T_\infty^4) \end{aligned} \tag{7}$$

Subscript w, r, and ∞ denote wall, recovery, and free stream; $\rho_e U_e C_H$ is the convective coefficient; B' terms are blowing parameters; σ, ε are radiative constants. Downward conduction balances aerothermal input as the convective term is modified by blowing and net radiation $-\sigma\varepsilon(T_w^4 - T_\infty^4)$ giving Eq. (7).

Recession speed follows from the normalized char mass loss rate:

$$B' = B'_c + B'_g, \qquad B'_g = \frac{\dot{m}_{g|_w}}{\rho_e U_e C_H}, \qquad \dot{s} = \frac{\rho_e U_e C_H B'_c}{\rho_s} \tag{8}$$

The nondimensional mass-loss parameters scale the species mass fluxes with the convective coefficient of heat transfer. Char removal sets the recession rate by mass conservation at the surface: $\dot{s}\rho_s = (\rho_e U_e C_H)B'_c$.

For each decomposing solid component $i \in \{A, B, C\}$, a local conversion based on densities:

$$\alpha_i = \frac{\rho_{v,i} - \rho_i}{\rho_{v,i} - \rho_{c,i}}, \qquad 0 \leq \alpha_i \leq 1 \tag{9}$$

Construct a dimensionless progress variable mapping density from the virgin to the char state. Adopt a general mechanism-independent rate form:

$$\frac{\partial \rho_i}{\partial t} = -(\rho_{v,i} - \rho_{c,i})\frac{d\alpha_i}{dt} \tag{10}$$

Below, $f_i(\alpha)$ is a smooth structural function, while $E_i(\alpha)$ and $A_i(\alpha)$ are obtained from multi-rate TGA via the integral FWO method. For constant heating rate $\beta = dT/dt$ and fixed conversion α, the FWO relation (Doyle approximation) is:

$$\frac{d\alpha_i}{dt} = A_i(\alpha_i) f_i(\alpha_i) \exp\left[-\frac{E_i(\alpha_i)}{RT}\right] \tag{11}$$

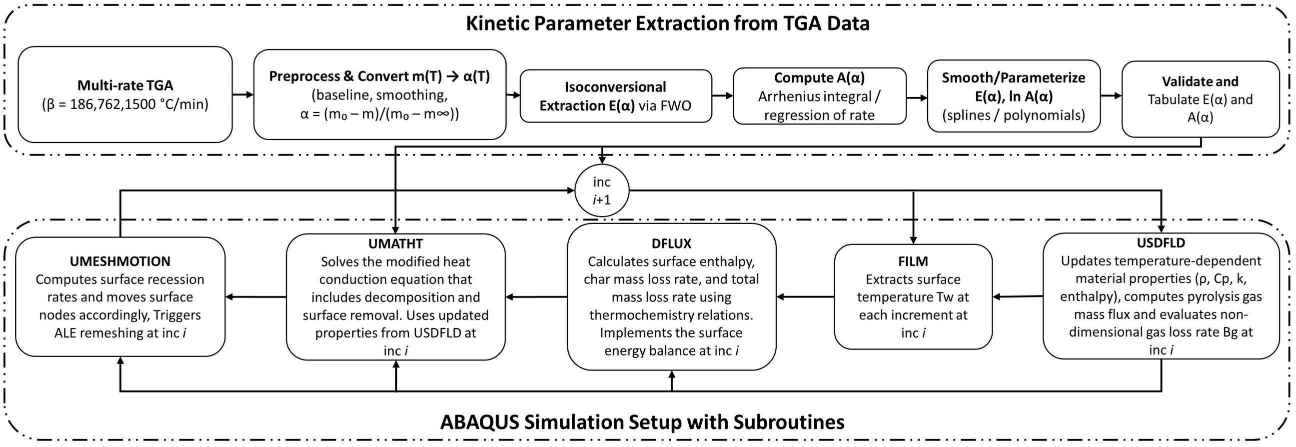

Figure 2: Workflow for isoconversional kinetic parameter extraction and integration into the Abaqus `UMATHT` subroutine.

The conversion integral allows extraction of $A(\alpha)$, while $E(\alpha)$ is identified from the intercept and slope, respectively, of $\ln\beta$ versus $1/T_\alpha$ plots:

$$\ln\beta = \ln\left(\frac{A_i(\alpha)E_i(\alpha)}{R\,g_i(\alpha)}\right) - 1.052\frac{E_i(\alpha)}{RT_\alpha} - 5.331 \quad (12)$$

A straight line in $\ln\beta$ versus $1/T_\alpha$ whose slope identifies $E_i(\alpha)$ and intercept gives $A_i(\alpha)/g_i(\alpha)$.

$$g_i(\alpha) = \int_0^\alpha \frac{d\xi}{f_i(\xi)} \quad (13)$$

Finally, bulk-density evolution follows from mixture weighting:

$$\frac{\partial\rho}{\partial t} = \Gamma\left(\frac{\partial\rho_A}{\partial t} + \frac{\partial\rho_B}{\partial t}\right) + (1-\Gamma)\frac{\partial\rho_C}{\partial t} \quad (14)$$

$\partial\rho/\partial t$ is the total bulk density rate; Γ and $1-\Gamma$ weight the resin and reinforcement contributions.

3. Isoconversional Kinetic Model for PICA and Abaqus Implementation

This section details the complete workflow used to construct a conversion-dependent kinetic model for Phenolic Impregnated Carbon Ablator (PICA) from multi-rate thermogravimetric analysis (TGA), and to embed the resulting tabulated kinetics in `Abaqus` via a user subroutine. The approach follows the model-free isoconversional framework to obtain activation energy $E(\alpha)$ and pre-exponential factor $A(\alpha)$ as functions of conversion α, and validates the model by reconstructing TGA curves across heating rates before deployment in a coupled thermal–pyrolysis finite-element model.

3.1. Multi-rate TGA acquisition and preprocessing

The analysis uses heating-rate data derived from a high-rate pyrolysis configuration developed for PICA materials, in which the specimen is resistively heated between copper clamps while mass loss is measured using synchronized gas-analysis instrumentation[41]. In this setup, the sample's center region can be driven at 186, 762, and 1500 °C/min, with each condition repeated 3 to 5 times to ensure consistent heating and mass-loss trends. These rates are far above those of standard TGA, but they were purposely chosen to better match the rapid temperature rise typical of high-flux testing and entry environments, making the resulting kinetics more suitable for comparison with oxy-acetylene torch data than conventional low-rate TGA.

For each heating rate, the mass-loss curve $m(T,t)$ was recorded and exported. Prior to kinetic evaluation, the data were corrected for instrument drift and gas-phase buoyancy, and subjected to light smoothing by a Savitzky–Golay filter with a small window to minimize noise while preserving the decomposition shape.

The normalized conversion fraction was obtained from:

$$\alpha(t) = \frac{m_0 - m(t)}{m_0 - m_\infty} \quad (15)$$

where m_0 is the initial sample mass and m_∞ is the residual char mass. The conversion profiles $\alpha(t)$ were numerically differentiated to evaluate the reaction rate, $\frac{d\alpha}{dt}$ which was used both for the Friedman differential method and also as a diagnostic to confirm consistency across the different heating rates β.

3.2. Extract $E(\alpha)$ from multi-rate data

Activation energy $E(\alpha)$ was determined at fixed levels of α using both integral and differential isoconversional estimators over $\alpha \in [0.02, 0.98]$. Among the available approaches, the Flynn–Wall–Ozawa (FWO) method was emphasized because of robustness, simplicity, and compatibility with multi-rate TGA data. FWO averages over a temperature interval at fixed conversion, which makes it less sensitive to noise compared with the Friedman differential formulation, whose derivative amplifies scatter at low or high α.

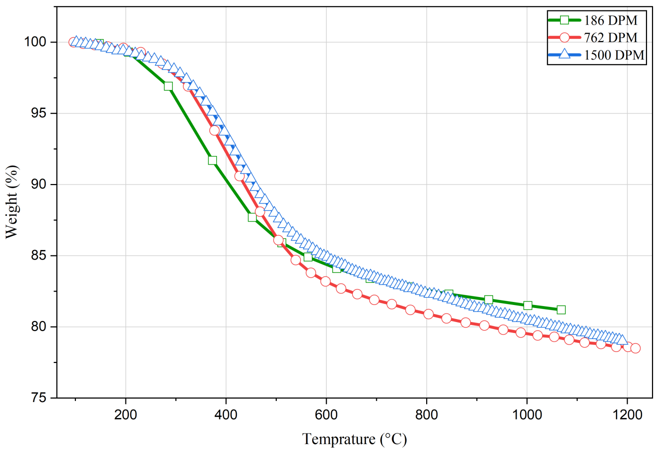

Figure 3: Multi-rate TGA curves for PICA at heating rates of 186, 762, and 1500 °C/min[41].

The FWO method is also model-independent, meaning it does not assume a specific reaction model. At each α, the kinetic parameters can be obtained directly from the linear regression slope of $\log \beta$ versus $1/T_\alpha$:

$$\log \beta = \log \left(\frac{AR}{E(\alpha)} \right) - \frac{0.4567 \cdot E(\alpha)}{R \cdot T_\alpha} \tag{16}$$

This regression is performed across three or more heating rates. In practice, FWO delivers smooth and stable $E(\alpha)$ profiles over the conversion range, whereas Friedman often produces scatter that complicates spline fitting or downstream tabulation. Because the present work requires polynomial or spline fits of $E(\alpha)$ and $A(\alpha)$ for use in `UMATHT`, this stability is of practical value. FWO is widely cited and supported by ICTAC guidelines and aerospace material studies.

This expression yields a local activation energy at each conversion level. Results from the integral and differential analyses were reconciled by rejecting poorly conditioned points and applying spline smoothing to construct a consensus profile. Activation energies were derived from multiple heating rates, and single-rate fits were excluded. The resulting $E(\alpha)$ profiles were refined by removing poorly conditioned intervals and applying spline smoothing to obtain a continuous curve.

For reference, the general isoconversional framework expresses the rate of conversion as

$$\frac{d\alpha}{dt} = A(\alpha) f(\alpha) \exp \left(-\frac{E(\alpha)}{RT} \right) \tag{17}$$

3.3. Determine $A(\alpha)$ (effective) and parameterize

Once $E(\alpha)$ had been established, the effective pre-exponential factor $A(\alpha)$ was determined by two complementary approaches. In the first, the Arrhenius integral was evaluated over narrow conversion intervals using the measured times $(t_{\text{start}}, t_{\text{end}})$ at each heating rate. In the second, $A(\alpha)$ was obtained by linear regression of

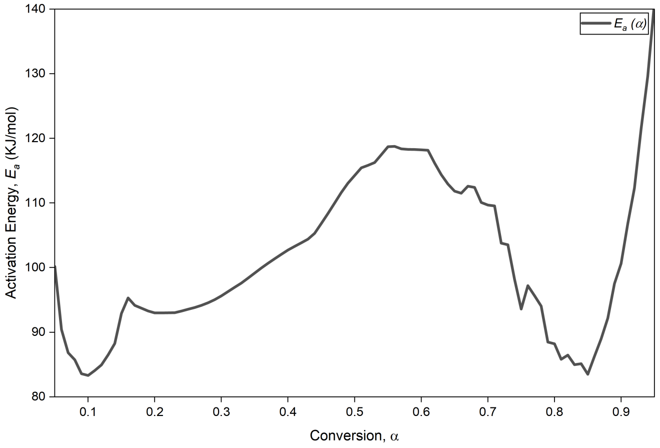

Figure 4: Conversion-dependent activation energy $E(\alpha)$ derived from the FWO method.

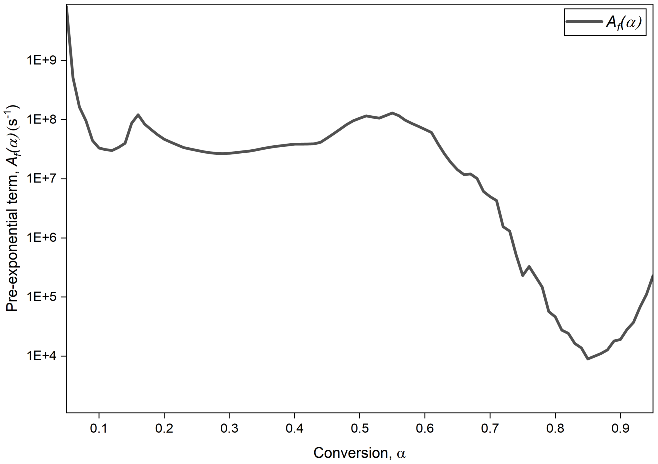

Figure 5: Conversion-dependent pre-exponential factor $A(\alpha)$ derived from tabulated isoconversional coefficients.

$$\ln \left(\frac{d\alpha}{dt} \right) + \frac{E(\alpha)}{RT} \tag{18}$$

against $\ln f(\alpha)$, where the reaction model was approximated as $f(\alpha) \approx (1 - \alpha)^m$ with a nominal order of $m = 1$.

Both procedures generated tabulated values of $\ln A(\alpha)$, which were subsequently smoothed using cubic splines subject to monotonicity constraints in order to eliminate spurious oscillations. The final outcome was a set of tabulated coefficients $\{\alpha_k,\ E(\alpha_k),\ \ln A(\alpha_k)\}$ resolved on a grid of $\Delta\alpha \approx 0.01 - 0.02$.

Additional calibrations using $m = 0.5$ and $m = 2$ yielded reconstructed multi-rate TGA curves with mean $|\Delta\alpha| < 0.02$ across $0.05 \leq \alpha \leq 0.95$. When these alternative pre-factors were used in the ablation simulation, the predicted surface temperature varied by less than 2% and the recession rate by less than 5%. These small differences demonstrate that the analysis is insensitive to the specific choice of m in $f(\alpha)$.

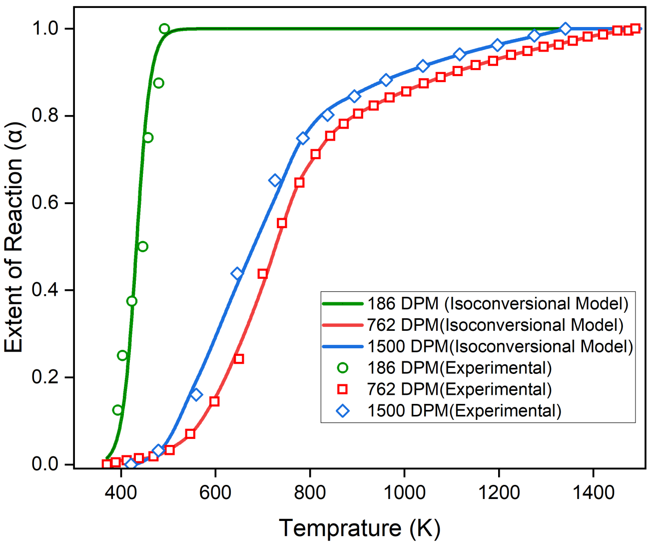

Figure 6: Isoconversional data compared with experimental data.

3.4. Validation against the calibration TGA set

The tabulated kinetic coefficients $\{E(\alpha), A(\alpha)\}$ were employed to forward-simulate non-isothermal TGA curves at each heating rate by integrating equation 18 with the experimental $T(t)$ and comparing with measured $\alpha(T)$. Then $\alpha(T)$ is reconstructed for each heating rate using the tabulated $\{E(\alpha), A(\alpha)\}$ and checked (i) mean $|\Delta\alpha| < 0.02$ over 0.05–0.95, (ii) peak-rate temperature within ≈ 3 °C of data, and (iii) absence of nonphysical spikes at high α. This mirrors recommended practice for isoconversional analysis and ensures the tabulation resolution is sufficient, a known sensitivity in this approach.

4. Results and Discussion

4.1. Numerical verification and mesh sensitivity

By applying 10×0.05 mm and 10×0.1 mm domain mesh sizes near the flame-exposed surface, the mesh sensitivity of the proposed ablation model was evaluated. As shown in the Fig.7, recession histories predicted using FIAT, Arrhenius kinetics, and FWO isoconversional kinetics are compared. The Arrhenius-based ABAQUS results obtained with finer mesh resolution (mesh size of 0.06 mm) closely match the FIAT predictions over the full heating duration, including at the final exposure time of 600 s, despite the use of finite-element and finite-volume formulations, respectively. This agreement indicates a weak dependence of the Arrhenius-based recession response on further mesh refinement.

In contrast, simulations employing FWO isoconversional kinetics predict systematically lower recession rates. At 600 s, the difference between the two mesh resolutions for the FWO cases remains on the order of approximately 1%, indicating that the effect of mesh refinement on the predicted recession depth is negligible. These results demonstrate that the recession response obtained using ABAQUS-based FWO kinetic modeling is effectively mesh-converged within the investigated resolution range.

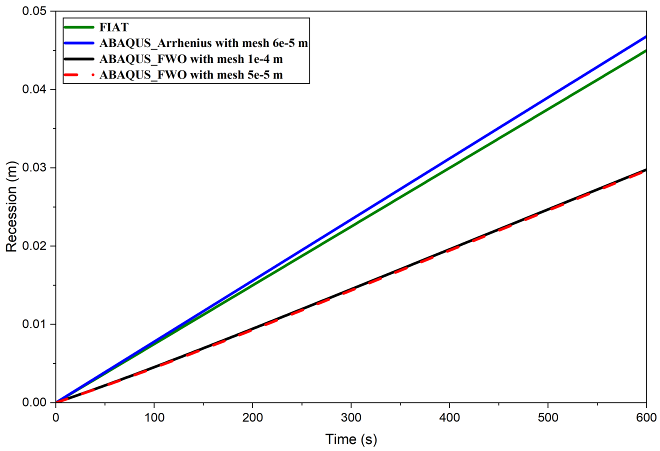

Figure 7: Surface-recession histories predicted using ABAQUS with Arrhenius and FWO isoconversional kinetics for two mesh resolutions, compared with FIAT .

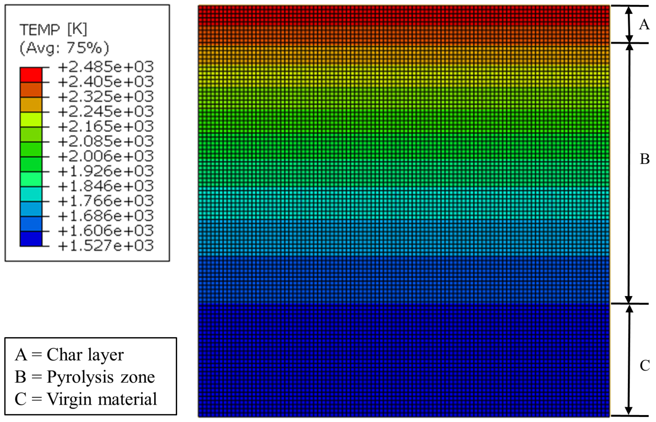

Figure 8: One-dimensional thermal response simulation of PICA using Abaqus with FWO method integration.

4.2. Thermal Field and Internal Response

Fig.8 shows the depthwise progression of heating for 1D PICA in `Abaqus`. Zone A indicates char-layer formation at the top, with a maximum temperature of about 2485 K, where heat flux is applied via the subroutines. Moving downward into Zone B, the color shift indicates a strong thermal gradient. Zone C at the bottom is where heat has not fully penetrated.

The FWO model, by incorporating α-dependence, slows decomposition during mid-stages and stabilizes the surface. This produces a more gradual char-front progression compared with the Arrhenius model and remains consistent with observations from experimental data.

4.3. Ablation Depth Kinetics

Fig.10 compares FWO and Arrhenius simulations with experimental ablation depth for a 7-mm-thick exposed sample. Experimentally, 7 mm of ablation occurs at 30 s. Both

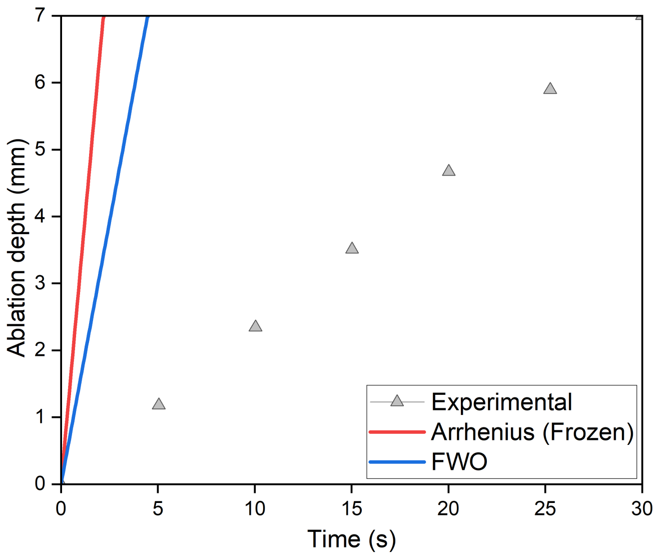

Figure 9: Evaluation of ablation depth predicted by FWO vs. Arrhenius relative to experimental data.

models predict faster ablation than measured. The isoconversional model reaches 7 mm in 4.4 s, while the Arrhenius model reaches 7 mm in 2.6 s. The FWO model overpredicts recession by a factor of 6.82 and reduces the error by 39% compared with the Arrhenius model, which overpredicts by 14.08×.

The mid-time curvature in the isoconversional curve marks a significant transition. As devolatilization decreases and the char layer grows, net conductivity drops, and the same surface heating produces less in-depth temperature rise. This reduces the instantaneous char-consumption term in the surface balance and flattens the depth curve without any change to external heating. This behavior is captured by conversion-dependent kinetics but not by a constant-barrier formulation.

4.4. Surface Temperature

The simulation predicts the outer-surface temperature reasonably well after 9 s, at which point the slope becomes flat. Although a gap remains, the root-mean-square error is about 105 K, indicating modest surface temperature error. However, temperatures measured by in-depth thermocouples show large deviations from model predictions. The experimental temperature rises more sharply and reaches higher values earlier, whereas the FWO in-depth temperature response shows more gradual heating and reaches maximum temperature with a delay.

The experimental surface temperature exhibits a wavy pattern not captured by the model, which is typical of drift during char ablation. The modeled temperature curves maintain the correct trend with respect to load: higher boundary-flux cases reach higher plateau temperatures sooner, and moderate cases behave similarly to mid-range experiments.

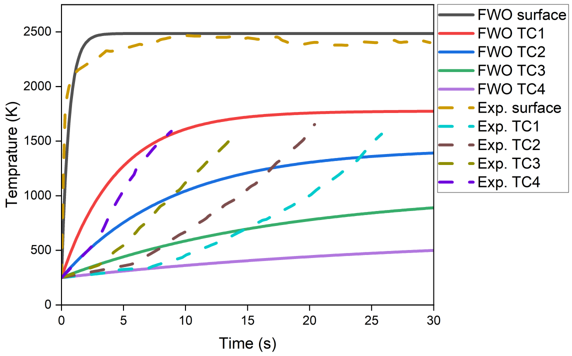

Figure 10: ABAQUS FWO-case simulations compared with experimental temperature histories at the surface and four thermocouple positions.

Table 1
RMSE evaluation of Arrhenius and FWO kinetic models

Model	RMSE (K)	RMSE (mm/s)
Arrhenius Model	364.97	1.2070
FWO Model	50.95	0.7339

This consistent ordering suggests that remaining discrepancies are likely due to surface boundary-condition effects rather than bulk material response.

4.5. Surface Temperature and Recession Validation of Charring Ablation Models for PICA

Before incorporation into `UMATHT`, the FWO model was first validated independently to confirm that its predicted decomposition and recession behavior matched the experimental trend. A second verification was then performed after implementing the kinetics in `ABAQUS` to ensure that the coupled thermal–ablation response was preserved. As shown in Table 1, the recession results confirm that the integrated model maintains the expected performance of the FWO formulation.

The FWO formulation yields a substantially lower Root Mean Square Error (RMSE) than the Arrhenius model, reducing the recession-rate prediction error by approximately 39% and providing a closer match to the experimental recession rate of 0.24 mm/s. This improvement reflects a closer match to the experimental recession behavior and a more accurate representation of effective decomposition kinetics. The model therefore captures the progression of the ablation front with higher fidelity across the examined heating range.

Surface temperature is treated separately because it is directly measurable by infrared pyrometry and provides an independent anchor for validating the thermal response of PICA under high heat flux. Unlike subsurface thermocouples, the surface signal reflects the actual wall energy balance and governs pyrolysis onset, char formation, and early recession behavior. The FWO model lowers the surface-temperature RMSE by about 86% relative to the Arrhenius

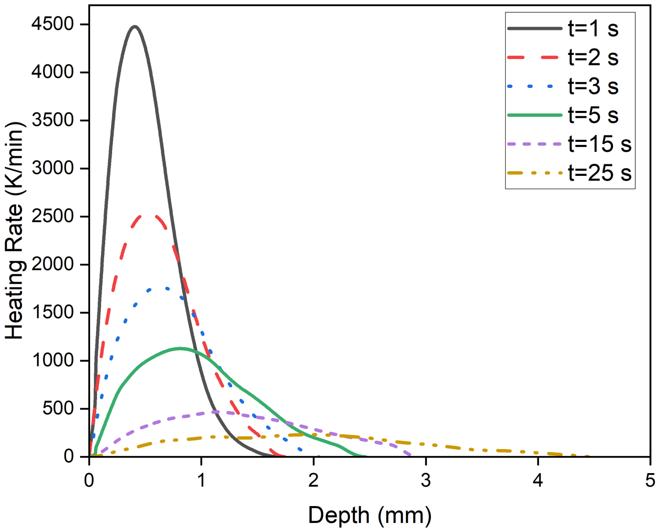

Figure 11: Heating rate variation as a function of depth over time.

prediction, indicating a far closer reproduction of the measured wall-temperature field. By isolating this observable, the comparison cleanly distinguishes thermal-model fidelity from downstream errors in decomposition or recession-rate prediction.

4.6. In-depth Heating Rate

Exposure to imposed surface flux and conduction into the depth produces different heating rates. The heating rate decreases sharply with depth due to rapid attenuation through the ablator. Near 0.5 mm depth, the external surface shows the most intense gradient from radiation and gas flow. By 2 s, both the magnitude and steepness of the peak decrease, and the curves flatten. The layer heats rapidly at first and then stabilizes as ablation and pyrolysis develop. Because the model reproduces char-layer formation, the curves shift deeper with time. Heat transfer decreases as the char acts as an insulating barrier. Variable activation energy causes spatially varying reaction rates and depth-dependent heating.

4.7. Boundary Energy Balance Cross Check

A steady-state control volume wrapped around the surface clarifies the temperature–recession trade. The convective term $(\rho_e U_e C_H)(h_r - h_w)$ delivers energy to the wall. Part of that energy is carried away by mass removal, $\rho_e U_e C_H B'_c$, and part is re-radiated, $\sigma\epsilon(T_w^4 - T_\infty^4)$. When these terms balance, the surface temperature sits on a plateau. The overall mass flux B is then set by the enthalpy difference rather than the in-depth details. Analyses of the same torch setup show that no single coefficient $\rho_e U_e C_H$ simultaneously matches both the measured plateau and the measured recession. A coefficient that fits T_w drives B' too high, or vice versa.

In the surface-temperature histories, the correct plateau level is reached earlier than in experiments, indicating a stiff boundary closure. Adjusting only the convective coefficient introduces compensating errors. Weakening the boundary slows the approach to the plateau but shifts the plateau itself unless wall-chemistry terms are modified simultaneously. A finite-rate wall-chemistry correction shifts the effective term without altering T_w. This delays the approach while keeping the plateau nearly unchanged—exactly the behavior needed to match profiles through the thickness.

Although the isoconversional formulation substantially reduces the recession bias relative to a constant-barrier Arrhenius model, the remaining discrepancy indicates that bulk-pyrolysis kinetics are not the sole source of error. In particular, uncertainties in surface energy-balance closure and finite-rate surface chemistry can influence the partitioning between surface temperature and mass loss under oxy-acetylene heating. The present results therefore isolate the effect of conversion-dependent decomposition kinetics while deliberately holding boundary modeling constant.

Model sensitivity and applicability

The sensitivity of the predicted response to modeling assumptions was assessed through internal consistency checks rather than additional parameter sweeps. Changing the reaction model exponent produced changes of less than 5% in the recession rate, while the surface temperature changed by less than 2%, indicating weak dependence on the exact reaction form. As the heat flux increased, the pattern of temperature plateaus and recession rates remained nearly constant, indicating that the observed improvements arise from conversion-dependent kinetics rather than from variations in boundary conditions. These observations suggest that the proposed model is reliable within the experimentally tested heating conditions, while at substantially higher heating rates, detailed surface chemistry and coupled flow effects will be required.

5. Conclusion

In this study, a finite element simulation was conducted for a one-dimensional charring ablator exposed to an oxy-acetylene torch to evaluate the effect of kinetic models on predicted surface temperature and recession. Both a traditional Arrhenius formulation and an isoconversional Flynn–Wall–Ozawa (FWO) description, obtained from multi-rate TGA, were implemented into the heat-transfer governing equations through user subroutines.

The Arrhenius-based results reproduced the experimental surface temperature reasonably well. Predicted values increased from approximately 1600 K at 0.1 kg/(m^2·s) to 2600 K at 2.2 kg/(m^2·s), lying between the two experimental reference levels of 2250 K and 2500 K. However, the corresponding surface-recession rates were significantly higher than measured, with values ranging from 0.14 mm/s at 0.08 kg/(m^2·s) to 2.45 mm/s at 2.2 kg/(m^2·s). These predictions are roughly three to ten times larger than the experimental mean of 0.24 mm/s.

When the FWO model was introduced, the conversion-dependent kinetics increased in-depth gas release. This enhanced surface blowing and reduced net char consumption.

As a result, the predicted recession was lowered by 15–40% compared with the Arrhenius model, with values reduced to 0.12 mm/s at 0.08 kg/(m^2·s) and 1.6 mm/s at 2.2 kg/(m^2·s). At the same time, the surface temperature decreased by 60–120 K in the range of 0.6–1.3 kg/(m^2·s), providing improved agreement with the experimental temperature band.

Despite these improvements, the simulations could not achieve a single coefficient of heat transfer that simultaneously matched both surface temperature and recession measurements. This discrepancy highlights the need for refinements beyond bulk-pyrolysis kinetics, including finite-rate surface chemistry, more accurate torch characterization, and coupled CFD/FEA approaches. Nonetheless, the FWO isoconversional kinetics provide a more realistic material description than a single Arrhenius parameter set and reduce the inconsistencies observed in earlier predictions.

CRediT authorship contribution statement

Kalid Kassa: Writing – original draft, Conceptualization, Software, Writing – review & editing, Methodology, Formal analysis. **Abrar H. Baluch**: Writing – review & editing, Supervision, Methodology, Investigation, Funding acquisition. **Qasem Ahmed Drmosh**: Writing – review & editing, Methodology, Investigation, Conceptualization. **Suhail Hyder Vattathurvalappil**: Methodology, Conceptualization, Investigation. **Sheriffdeen Anafi**: Software, Methodology, Investigation.

Acknowledgment

This work was supported by the Interdisciplinary Research Center for Aviation and Space Exploration, King Fahd University of Petroleum and Minerals (KFUPM) funded by the internal grants INAE2402.

References

[1] K. K. Sarswat and N. Mehta. Thermogravimetric insights into decomposition and lifetime prediction in stsi glass-ceramics. *npj Materials Degradation*, 9:146, 2025. doi: 10.1038/s41529-025-00665-9.

[2] A. J. Amar, A. B. Oliver, B. S. Kirk, G. Salazar, and J. Droba. Overview of the charring ablator response (char) code. In *Proceedings of the 46th AIAA Thermophysics Conference*, 2016. doi: 10.2514/6.2016-3385. AIAA Paper 2016-3385.

[3] Y. K. Chen and F. S. Milos. Ablation and thermal response program for spacecraft heatshield analysis. *Journal of Spacecraft and Rockets*, 36(3):475–483, 1999. doi: 10.2514/2.3469.

[4] Y. K. Chen and F. S. Milos. Multidimensional finite volume fully implicit ablation and thermal response code. *Journal of Spacecraft and Rockets*, 55(4):914–927, 2018. doi: 10.2514/1.A34184.

[5] J. A. Dec, R. D. Braun, and B. Laub. Ablative thermal response analysis using the finite element method. *Journal of Thermophysics and Heat Transfer*, 26(2):201–212, 2012. doi: 10.2514/1.T3694.

[6] M. Natali, J. M. Kenny, and L. Torre. Science and technology of polymeric ablative materials for thermal protection systems and propulsion devices: A review. *Progress in Materials Science*, 84:192–275, 2016. doi: 10.1016/j.pmatsci.2016.08.003.

[7] J. B. E. Meurisse, J. Lachaud, F. Panerai, C. Tang, and N. N. Mansour. Multidimensional material response simulations of a full-scale tiled ablative heatshield. *Aerospace Science and Technology*, 76:497–511, 2018. doi: 10.1016/j.ast.2018.01.013.

[8] J. Lachaud and N. N. Mansour. Porous-material analysis toolbox based on openfoam and applications. *Journal of Thermophysics and Heat Transfer*, 28:191–202, 2014. doi: 10.2514/1.T4262.

[9] E. Poloni et al. Carbon ablators with porosity tailored for aerospace thermal protection during atmospheric re-entry. *Carbon*, 195:80–91, 2022. doi: 10.1016/j.carbon.2022.03.062.

[10] E. Poloni et al. An open carbon–phenolic ablator for scientific exploration. *Scientific Reports*, 13:40351, 2023. doi: 10.1038/s41598-023-40351-x.

[11] C. T. Quinn, D. N. Pickard, and N. N. Mansour. Validation of a charring ablator material response code against oxyacetylene torch experiments on pica samples. In *Proceedings of the AIAA SciTech 2024 Forum*, 2024. doi: 10.2514/6.2024-0862. AIAA Paper 2024-0862.

[12] M. E. Ewing et al. Numerical modeling of ablation heat transfer. *Journal of Thermophysics and Heat Transfer*, 27(4):615–632, 2013. doi: 10.2514/1.T4164.

[13] S. Ali et al. Microstructural and thermal analysis of alumina modified carbon/phenolic composites after ablation testing. *Journal of Composite Materials*, 57:885–896, 2023. doi: 10.1177/00219983221147389.

[14] S. Ahmad et al. A comparative study on the effect of carbon-based and ceramic additives on the properties of fiber reinforced polymer matrix composites for high temperature applications. *Ceramics International*, 47:33956–33971, 2021. doi: 10.1016/j.ceramint.2021.08.356.

[15] I. Gallegos et al. Revealing nanoscale mechanisms of pyrolysis at phenolic resin/carbon fiber interface. *Journal of Materials Science*, 60:5106–5124, 2025. doi: 10.1007/s10853-025-10769-x.

[16] K. Hirano and M. Asami. Phenolic resins—100 years of progress and their future. *Reactive and Functional Polymers*, 73:256–269, 2013. doi: 10.1016/j.reactfunctpolym.2012.07.003.

[17] K. L. Joshi, S. Raman, and A. C. Van Duin. Connectivity-based parallel replica dynamics for chemically reactive systems. *Journal of Physical Chemistry Letters*, 4(21):3792–3797, 2013. doi: 10.1021/jz4019223.

[18] Y. Wang, T. K. Risch, and J. H. Koo. Assessment of a one-dimensional finite element charring ablation material response model for phenolic-impregnated carbon ablator. *Aerospace Science and Technology*, 91: 301–309, 2019. doi: 10.1016/j.ast.2019.05.039.

[19] SIMULIA Dassault Systèmes. *Abaqus User Subroutines Reference Guide*, 2016. URL `https://www.3ds.com/products-services/simulia/products/abaqus/`.

[20] J. H. Flynn and L. A. Wall. General treatment of the thermogravimetry of polymers. *Journal of Research of the National Bureau of Standards*, 70A:487–523, 1966. doi: 10.6028/jres.070A.043.

[21] H. L. Friedman. Kinetics of thermal degradation of char-forming plastics from thermogravimetry. *Journal of Polymer Science*, 6:183–195, 1964. doi: 10.1002/polc.5070060121.

[22] H. E. Kissinger. Reaction kinetics in differential thermal analysis. *Analytical Chemistry*, 29:1702–1706, 1957. doi: 10.1021/ac60131a045.

[23] T. Ozawa. A new method of analyzing thermogravimetric data. *Bulletin of the Chemical Society of Japan*, 38:1881–1886, 1965. doi: 10.1246/bcsj.38.1881.

[24] S. Vyazovkin, A. K. Burnham, et al. Ictac kinetics committee recommendations for performing kinetic computations on thermal analysis data. *Thermochimica Acta*, 520:1–19, 2011. doi: 10.1016/j.tca.2011.03.034.

[25] H. K. Tran, C. E. Johnson, D. J. Rasky, F. C. L. Hui, et al. Phenolic impregnated carbon ablators (pica) as thermal protection systems for discovery missions. Technical Report TM-110440, NASA, 1997. URL `https://archive.org/details/NASA_NTRS_Archive_19970017002`.

[26] M. E. Ewing and B. Pincock. Heat transfer modeling of a charring material using isoconversional kinetics. *Heat Transfer Engineering*, 38:1189–1197, 2017. doi: 10.1080/01457632.2016.1239939.

[27] K. A. Trick, T. E. Saliba, and S. S. Sandhu. A kinetic model of the pyrolysis of phenolic resin in a carbon/phenolic composite. *Carbon*, 35:393–401, 1997. doi: 10.1016/S0008-6223(97)89610-8.

[28] A. Langenais, J. Aubrée, et al. Numerical simulation of flight effects on afterburning rocket exhaust plumes. HAL Preprint, 2024. URL `https://hal.science/hal-04602384`.

[29] M. Natali et al. Ablation modeling of state-of-the-art epdm based elastomeric heat shielding materials for solid rocket motors. *Computational Materials Science*, 111:460–480, 2016. doi: 10.1016/j.commatsci.2015.09.050.

[30] P. Schrooyen et al. Two-way coupled simulations of stagnation-point ablation with transient material response. *International Journal of Thermal Sciences*, 134:639–652, 2018. doi: 10.1016/j.ijthermalsci.2018.08.014.

[31] S. Gordon and B. J. McBride. *Chemical Equilibrium with Applications*. 2017.

[32] R. A. Ahmad. Convective heat transfer in the reusable solid rocket motor of the space transportation system. *Heat Transfer Engineering*, 26:30–45, 2005. doi: 10.1080/01457630500248554.

[33] E. S. Shin, S. J. Kim, and J. I. Kim. Coupled thermal/structural analysis of mechanical ablation by domain/boundary decomposition method. *Journal of the Korean Society for Aeronautical and Space Sciences*, 39(1):1–8, 2011. doi: 10.5139/JKSAS.2010.39.1.1.

[34] F. Grigat et al. Spallation of carbon ablators in arcjet facility experiments. *Journal of Thermophysics and Heat Transfer*, 36(5): 624–635, 2022. doi: 10.2514/1.T6587.

[35] S. Löhle et al. Assessment of high enthalpy flow conditions for re-entry aerothermodynamics in the plasma wind tunnel facilities at irs. *CEAS Space Journal*, 14:395–406, 2021. doi: 10.1007/s12567-021-00396-y.

[36] T. White et al. Thermal protection system materials for sample return missions. 2021. doi: 10.3847/25c2cfeb.72d83582.

[37] O. Uyanna and H. Najafi. Thermal protection systems for space vehicles: A review on technology development, current challenges and future prospects. *Acta Astronautica*, 176:341–356, 2020. doi: 10.1016/j.actaastro.2020.06.047.

[38] I. Sakraker, O. Chazot, and J. P. Carvalho. Performance of cork-based thermal protection material p50 exposed to air plasma. *CEAS Space Journal*, 14:377–393, 2022. doi: 10.1007/s12567-021-00395-z.

[39] R. Bottacchiari, L. Borgese, L. Paglia, et al. Carbon–phenolic ablators modified by ceramic nanofilms deposited via atomic layer deposition. *Coatings*, 14:1551, 2024. doi: 10.3390/coatings14121551.

[40] A. Cuadra, C. Huete, and M. Vera. Combustion toolbox: An open-source thermochemical code. arXiv:2409.15086, 2024.

[41] B. K. Bessire and T. K. Minton. Decomposition of phenolic impregnated carbon ablator (pica) as a function of temperature and heating rate. *ACS Applied Materials & Interfaces*, 9:25057–25067, 2017. doi: 10.1021/acsami.7b03919.